PHOTONICS Research

Electrical manipulation of lightwaves in the uniaxially strained photonic honeycomb lattices under a pseudomagnetic field

Zhipeng Qi,[1,†] Hao Sun,[2,†] Guohua Hu,[3,5] Chunyu Deng,[3] Wanghua Zhu,[3] Bo Liu,[1,6] Ying Li,[1] Shaopeng Liu,[1] Xuechao Yu,[4] and Yinping Cui[3,7]

[1]School of Physics and Optoelectronic Engineering, Nanjing University of Information Science & Technology, Nanjing 210044, China
[2]The Institute for Functional Intelligent Materials (I-FIM), National University of Singapore, Singapore 117544, Singapore
[3]Advanced Photonics Center, School of Electronic Science and Engineering, Southeast University, Nanjing 210096, China
[4]Key Laboratory of Multifunctional Nanomaterials and Smart Systems, Suzhou Institute of Nano-Tech and Nano-Bionics, Chinese Academy of Sciences, Suzhou 215123, China
[5]e-mail: photonics@seu.edu.cn
[6]e-mail: bo@nuist.edu.cn
[7]e-mail: cyp@seu.edu.cn
[†]These authors contributed equally to this work.

Received 24 January 2023; revised 8 May 2023; accepted 10 May 2023; posted 11 May 2023 (Doc. ID 486329); published 26 June 2023

The realization of pseudomagnetic fields for lightwaves has attained great attention in the field of nanophotonics. Like real magnetic fields, Landau quantization could be induced by pseudomagnetic fields in the strain-engineered graphene. We demonstrated that pseudomagnetic fields can also be introduced to photonic crystals by exerting a linear parabolic deformation onto the honeycomb lattices, giving rise to degenerate energy states and flat plateaus in the photonic band structures. We successfully inspire the photonic snake modes corresponding to the helical state in the synthetic magnetic heterostructure by adopting a microdisk for the unidirectional coupling. By integrating heat electrodes, we can further electrically manipulate the photonic density of states for the uniaxially strained photonic crystal. This offers an unprecedented opportunity to obtain on-chip robust optical transports under the electrical tunable pseudomagnetic fields, opening the possibility to design Si-based functional topological photonic devices.

https://doi.org/10.1364/PRJ.486329

1. INTRODUCTION

In 2D electronic systems, a strong external magnetic field is always needed to observed the quantum Hall effect (QHE) [1], leading to degenerate Landau levels by breaking the time-reversal symmetry [2]. Given that the Fermi level lies between two adjacent Landau levels, 2D electronic systems exhibit topological properties that insulate in the bulk while conducting on the edges [3]. Like real magnetic fields, the customized strain-induced deformation on the honeycomb lattices of graphene could generate a gauge field that is a pseudomagnetic field ($\boldsymbol{B}_s$) [4]. In the presence of $\boldsymbol{B}_s$, the Landau quantization occurs at the energy levels near the Dirac points without violating the time-reversal symmetry [5–7]. Furthermore, $\boldsymbol{B}_s$ can be much larger than the real magnetic fields when a high mechanical strain is applied [8–15].

In addition to electronic systems, studies of photonic Landau levels are also of significant interest, showing great promise in the enhancement of light–matter interactions [16–20] and the realization of robust optical transports [21–24]. Unlike electrons, photons are uncharged and therefore insensitive to real magnetic fields. Except for some specific optical media like metamaterials [25–27], it is particularly difficult to attain photonic Landau levels in conventional optical materials or structures because of their inertness to the magnetic fields. Addressing this issue, recent developments in the Harper–Hofstadter (H–H) models such as resonator arrays [23,28] and flexible cavity systems [29] have paved the way to realize photonic Landau levels without external magnetic fields. Alternatively, one of the most straightforward methods is to use synthetic magnetic fields (i.e., $\boldsymbol{B}_s$) by engineering the strain onto the photonic honeycomb lattices [30]. $\boldsymbol{B}_s$ can be introduced to the graphene-like photonic crystals (PhCs) by carefully modifying the nearest-neighbor hopping parameters across the honeycomb lattices [31]. The generated Landau levels in the strained PhCs feature quasi-flat bands with a certain energy spacing, analogous to the strain-engineered graphene monolayer. In particular, $\boldsymbol{B}_s$ is mainly dominated by the applied

strain (i.e., the lattice deformation), which is convenient for control and manipulation.

In the optical systems, $\boldsymbol{B}_s$ was firstly demonstrated in the triaxially strained honeycomb lattices consisting of arrayed dielectric waveguides, yielding photonic Landau levels [32]. With this concept, a strain-induced gauge field and Landau quantization have also been achieved in acoustic crystals [33]. As reported by Jamadi *et al.* [34], both photonic Landau levels and helical edge states originating from $\boldsymbol{B}_s$ were directly observed in a uniaxially strained PhC on a Si chip. Even without applying the triaxial strains [35], the uniaxial hopping gradient can still generate uniform $\boldsymbol{B}_s$ [36,37], which is promising to establish topological photonic channels protected by helical states [38].

Recently, manipulating lightwaves in the nanostructures or integrated systems has played a crucial role in signal processing, real-time sensing, and data transferring [39–41]. As periodic configurations, PhCs display great potential in the flexible modulation of photons [42–44]. However, the control and manipulation of photonic band structures arising from strain-induced $\boldsymbol{B}_s$ have remained unexplored to the best of our knowledge. In this paper, we experimentally demonstrate the electrical manipulation of lightwaves in a uniaxially strained PhC with a honeycomb lattice on a silicon-on-insulator (SOI) substrate. Here, the $\boldsymbol{B}_s$-induced photonic band structures and density of states (DOS) are detected by measuring the optical transports based on the photonic option analogous to electrical probes; i.e., Si waveguides. With the integration of Si waveguides, gratings, and uniaxially strained PhCs, this on-chip interconnection becomes a versatile platform to study strain-engineered photonic lattices operating at telecom wavelengths and novel functional integrated optical devices, as we did in our previous work [45]. By taking advantage of a microdisk for unidirectional coupling, we show the existence of photonic helical snake states in the $\boldsymbol{B}_s$ heterostructure. Compared to graphene-based dynamic control [46–48], the electrical tunability of photons in such PhCs is enabled by a thermo-optic effect, providing an effective route to manipulate strain-induced $\boldsymbol{B}_s$ and photonic band structures.

2. RESULTS AND DISCUSSION

A. Applying the Uniaxial Strain onto the PhCs for $\boldsymbol{B}_s$

We start by considering the propagation of TE lightwaves in the plane of the PhC with a honeycomb lattice on an SOI substrate. Such a Si-based PhC is composed of 2D hexagonal arrayed nanostructures with a lattice constant (a_0) of nearly 408 nm, located on a 2 μm thick buried oxide (BOX) layer. As illustrated in Fig. 1(a), the unit cell of the proposed PhC contains two equivalent holes filled with SiO_2, with a thickness (h) of 220 nm and a diameter (d) of 130 nm for each hole. To protect the Si layer and to fabricate the heat electrodes, a 1.8 μm thick SiO_2 upper cladding layer is deposited onto the PhC configurations, as shown in Fig. 1(b). According to the Maxwell wave equations [49],

$$\nabla \times \left(\frac{1}{\varepsilon(r)}\nabla \times \vec{H}\right) + \mu_0\varepsilon_0\mu(r)\frac{\partial^2 \vec{H}}{\partial t^2} = 0, \tag{1}$$

$$\nabla \times \left(\frac{1}{\mu(r)}\nabla \times \vec{E}\right) + \varepsilon_0\mu_0\varepsilon(r)\frac{\partial^2 \vec{E}}{\partial t^2} = 0, \tag{2}$$

we could further obtain the eigenvalue function as

$$i\begin{pmatrix} 0 & \nabla\times \\ -\nabla\times & 0 \end{pmatrix}\begin{pmatrix} \vec{E} \\ \vec{H} \end{pmatrix} = \omega\begin{pmatrix} \varepsilon_0\varepsilon(r) & \chi \\ \chi^{\dagger} & \mu_0\mu(r) \end{pmatrix}\begin{pmatrix} \vec{E} \\ \vec{H} \end{pmatrix}. \tag{3}$$

Here, $\vec{E}$ and $\vec{H}$ symbolize the electric and magnetic components of the TE optical wave. μ_0 and ε_0 are the permeability and permittivity of vacuum, respectively. $\mu(r)$ and $\varepsilon(r)$ denote the relative permeability and permittivity of the PhC, varying

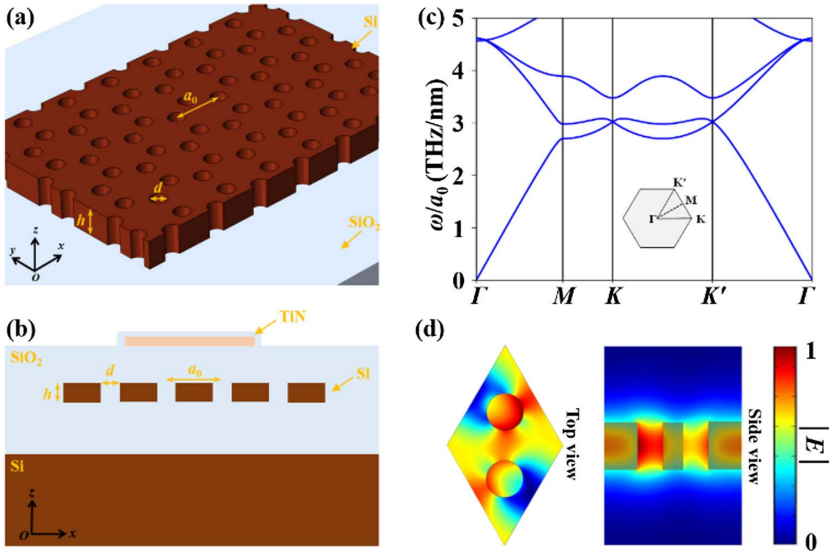

Fig. 1. PhC with the honeycomb lattice on an SOI substrate. (a) 3D schematic of the Si-based PhC with a lattice constant of 408 nm on the 2 μm thick SiO_2 layer. (b) Cross-sectional view of the PhC with the integration of heat electrodes. (c) Calculated band diagram for the unstrained PhC. The inset shows the FBZ of the PhC. (d) Top and side views of the electric field distributions in the unit cell of the lattice corresponded to the Dirac point.

periodically in space because of the arrayed nanostructures. Meanwhile, ω is the eigenfrequency and χ is the susceptibility tensor. The nonlinear optical effects induced by the propagating lightwaves in the Si-based PhC are very weak due to the lack of strong light interactions; therefore, they can be neglected in this study. Hence, the adopted Si and SiO_2 could be seen as isotropic optical materials, with the $\varepsilon(r)$ uniform in the x, y, and z directions. Owing to the large refractive index difference between the Si ($n_{Si} = 3.45$) and SiO_2 ($n_{SiO_2} = 1.44$) in the near-IR region, the SiO_2 holes in the Si layer act as photonic atoms. As shown in Fig. 1(c), the proposed PhC displays a pair of Dirac points, corresponding to K and K', at around 194 THz in the first Brillouin zone (FBZ). Since the hopping from each SiO_2 hole to its nearest neighbors can be seen as equal and spatially independent for the lattices with no deformations, the strong coupling and interaction between the conduction and valence bands give rise to Dirac cones. The appearing Dirac points (K and K') are under the protection of spatial inversion symmetry. Figure 1(d) shows that the excited electric field is not totally bounded by the SiO_2 hole but is dispersive in the bulk part within the hexagonal lattice, which reveals that the PhC can support the transports of photons at Dirac points. On the other hand, the propagating TE wave can be tightly confined by such PhC in the lateral direction without any leakages into the upper and lower SiO_2 cladding layers.

Generally, there are two kinds of strains that can induce $\boldsymbol{B}_s$ in the graphene-like honeycomb lattices: uniaxial [37,50,51] and triaxial strains [32]. In this work, we chose to perform linear gradient deformations (i.e., the uniaxial strain) along the opposite directions perpendicular to the zigzag edges of the proposed PhC [52], enabling the generation of large-area $\boldsymbol{B}_s$ for lightwaves and the creation of topologically protected photonic channels for helical states. Such a uniaxially strained PhC is shown in Fig. 2(a), where the hexagonal array of etched SiO_2 holes is arranged with a specific deformation but maintains mirror symmetry along the y axis. To perform band structure calculations, we constructed a tight-binding (TB) model based on the graphene nanoribbons (GNRs) for such zigzag-type photonic lattices [53], whose effective Hamiltonian can be expressed as

$$H = \sum t_{i,j} a_i b_j + \text{h.c.}, \tag{4}$$

and

$$[a_i, a_j] = i\delta_{ij}, \qquad [b_i, b_j] = i\delta_{ij}, \qquad [a_i, b_j] = 0, \tag{5}$$

where $t_{i,n}$ symbolizes the effective hopping amplitude. a_i and b_j are the operators of the annihilation of the optical modes on, respectively, the A and B sublattices, and δ_{ij} denotes Kronecker delta. The light coupling and interaction between the adjacent photonic atoms can be seen as the artificial carbon–carbon (C–C) bond. Then, we could obtain

$$d_{i,n} = \frac{1}{a_0}(a_0^2 + \varepsilon_{ab}(r_i)\delta_n^a \delta_n^b), \tag{6}$$

where δ_n are the three nearest neighbor bonds of photonic atoms without deformations (i.e., no strains) depicted as the green arrows in Fig. 2(a), and

$$\varepsilon_{ab}(r) = \frac{1}{2}(\partial_a u_b(r) + \partial_b u_a(r) + \partial_a h(r)\partial_b h(r)) \tag{7}$$

is the 2D strain tensor. $u(r)$ denotes the in-plane deformation, and $h(r)$ symbolizes the out-of-plane deformation, which is zero in our study. With the consideration of a strain-induced parabolic deformation

$$\vec{u}(x, y) = \begin{pmatrix} 0 \\ u_0 y^2 \end{pmatrix}, \tag{8}$$

the synthetic vector potential $\vec{A}$, which is given in unit $\hbar/e = 1$, is induced as [54]

$$\vec{A} = \begin{pmatrix} A_x \\ A_y \end{pmatrix} = -\beta \begin{pmatrix} \frac{u_0}{a_0} y \\ 0 \end{pmatrix}, \tag{9}$$

where β is the propagation constant of the lightwave. Then, the corresponding synthetic magnetic field (i.e., $\boldsymbol{B}_s$) could be generated [4] by

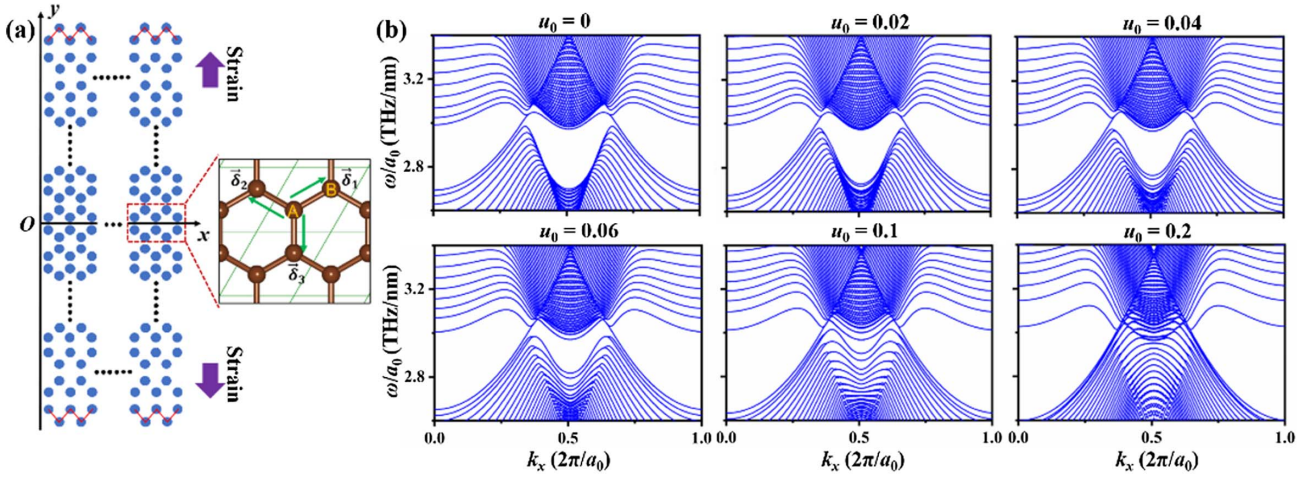

Fig. 2. Calculated band structures for the uniaxially strained PhC ribbons. (a) Sketch of the uniaxially strained PhC with a linear parabolic deformation along the y axis. The inset shows the honeycomb lattices composed of the photonic atoms. (b) Band diagrams for the uniaxially strained PhC ribbons with u_0 setting to be 0, 0.02, 0.04, 0.06, 0.1, and 0.2, respectively.

$$\overrightarrow{B_s} = \nabla \times \vec{A} = \beta \frac{u_0}{a_0} \vec{z}, \tag{10}$$

which should be uniform and perpendicular to the x–y plane. Moreover, the time-reversal symmetry is still conserved under such strain-induced $\boldsymbol{B}_s$, which could be attributed to the fact that $\boldsymbol{B}_s$ exhibits opposite signs in the K and K' valleys [13].

Figure 2(b) illustrates the numerically calculated band dispersions of the uniaxially strained PhCs with different u_0 (in units of $1/a_0$) based on the TB model of GNRs for 40 unit cells along the y axis. The periodic boundary conditions are set along the x axis. A linear gradient deformation of the honeycomb lattice along the y axis will cause the shift of the Dirac cones in the k_y direction, leading to the lift of the conical degeneracies [55]. Once the u_0 is enlarging, the band diagram of such PhC ribbon varies significantly: the photonic DOS increases greatly in the vicinity of the Dirac cones with the appearance of more flat plateaus in the energy states. Due to the wave group velocity $v_g = \partial\omega/\partial k$, the photons that correspond to the plateau states have zero v_g; therefore, they strongly localize in the bulk parts of the PhCs. This provides a great opportunity to detect the $\boldsymbol{B}_s$-modified photonic band structures by measuring the optical transports in the uniaxially strained PhCs.

B. Measurements of Optical Transports and Helical Snake States

The designed samples were prepared based on nanofabrication technology, which is totally CMOS-compatible. To implement the uniaxial strain onto the PhCs, we took advantage of electron beam lithography (EBL) and inductively coupled plasma (ICP) etching to pattern the deformed holes with parabolic displacements according to Eq. (8) on the top Si layer of the SOI substrate. Then, the SiO_2 upper cladding layer was deposited onto the patterned Si layer by low pressure chemical vapor deposition (LPCVD). Finally, the TiN electrodes were fabricated by using UV photolithography and electron beam evaporation (EBE). Compared to the electrical measurements of conventional 2D materials (e.g., the strained graphene [56]), we integrated the Si waveguides, gratings, and proposed PhCs for the optical tests, enabling the transport of photons totally on chip, as shown in Fig. 3(a). Analogous to the electrical probes, single-mode optical fibers were adopted to launch and detect the optical signals. Before coupling into the sample, the lightwave should be modulated by a polarization controller to ensure that only the fundamental TE mode can be excited in the Si rectangular 400 nm × 220 nm waveguide. In this system, the optical transports in the PhCs are measured in terms of the transmission spectra by using a tunable laser (TSL-710, Santec) with 0.05 nm wavelength resolution and an optical power meter (MPM-210, Santec).

As shown in Fig. 3(b), we manufactured SOI-based PhCs composed of, respectively, the pristine (i.e., without deformations) and the uniaxially strained photonic honeycomb lattices. With the u_0 setting at 0.04, the corresponding linear parabolic deformation was realized in our study, even though the fabrication errors were in the range of ±10 nm, providing a large enough $\boldsymbol{B}_s$ for the lightwave manipulation. To further investigate $\boldsymbol{B}_s$-induced photonic DOS and helical snake states, a 20.4 μm long straight domain wall was constructed by two PhC domains, whose linear gradient deformations were exerted along the opposite directions with the same $u_0 = 0.04$. As to Eqs. (9) and (10), these two PhC domains own equal, but opposite, $\boldsymbol{B}_s$, acting as magnetic heterostructures for charged particles. The width of each domain was 10.8 μm, which was sufficiently large to confine the bulk and snake state modes. Moreover, a pristine PhC with the same size as the uniaxially strained one was also fabricated for comparison. Figure 3(c) shows that the photonic band structure of the pristine PhC ribbon calculated by using the finite element method (FEM) is different with the π and π^* bands of graphene, where a Dirac point emerges due to the couplings of s, p_x, and p_y orbitals. Such a Dirac point is opened with the lift of the degeneracy under the $\boldsymbol{B}_s$ for the uniaxially strained PhC, where more discrete energy levels appear. Therefore, the number of photonic DOS peaks increases significantly in the frequency range of 190–200 THz when the uniaxial strain is applied to the pristine PhC. Note that the photonic DOS is inversely proportional to $\partial\omega/\partial k$ [57], revealing that the photonic DOS peaks are closely related to the flat energy states. Based on the analysis above, the inspiration of bulk modes corresponding to the flat plateaus could result in transmittivity dips. This can be also verified by the measurement results of the optical transports in our samples. Note that there is an agreement between the positions of the calculated photonic DOS peaks and the measured transmission dips. With the generation of degenerate energy states under the $\boldsymbol{B}_s$, more transmission dips emerged for the uniaxially strained PhC.

The domain wall in the uniaxially strained PhC consists of a row of undeformed honeycomb lattices, separating the whole PhC into two magnetic domains with the $\boldsymbol{B}_s$ of equal magnitudes but opposite directions that are kept normal to the chip surface. Similar to the topological waveguides based on valley PhCs [58], these two domains own opposite helicities of the motion. The introduction of such a domain wall was crucial to construct a topologically nontrivial photonic channel, which was expected to support the robust optical transports. As illustrated in Fig. 4(a), the inspired snake state mode was highly confined within the region around the domain wall compared to the bulk mode. If the domain wall is removed, the snake state can hardly exist because the deformation of $\boldsymbol{B}_s$-induced Landau level disappears, as explained in Ref. [59]. Figure 4(b) shows the field displacements of the Poynting vectors ($\boldsymbol{S}$) in the uniaxially strained PhC with the 3D finite-difference time-domain (FDTD) simulations. Inspired by an anticlockwise circularly polarized light source at the left end, the photon locked to the K valley starts with a clockwise rotation in the upper PhC domain ($y > 0$) under negative $\boldsymbol{B}_s$ and then enters the lower PhC domain ($y < 0$) with an anticlockwise rotation under the positive $\boldsymbol{B}_s$, resulting in the emergence of a snake optical mode in the middle of such two domains. The simulation results also show that the excitation of a snake state can be only fulfilled with an input frequency smaller than 187 THz; otherwise, no modes can be inspired, resulting in low transmittivity. Note that the snake state is identified by its winding number, which is a type of topological invariant. The winding numbers of the Landau levels have a direct correlation with physical observables, signifying that the helical

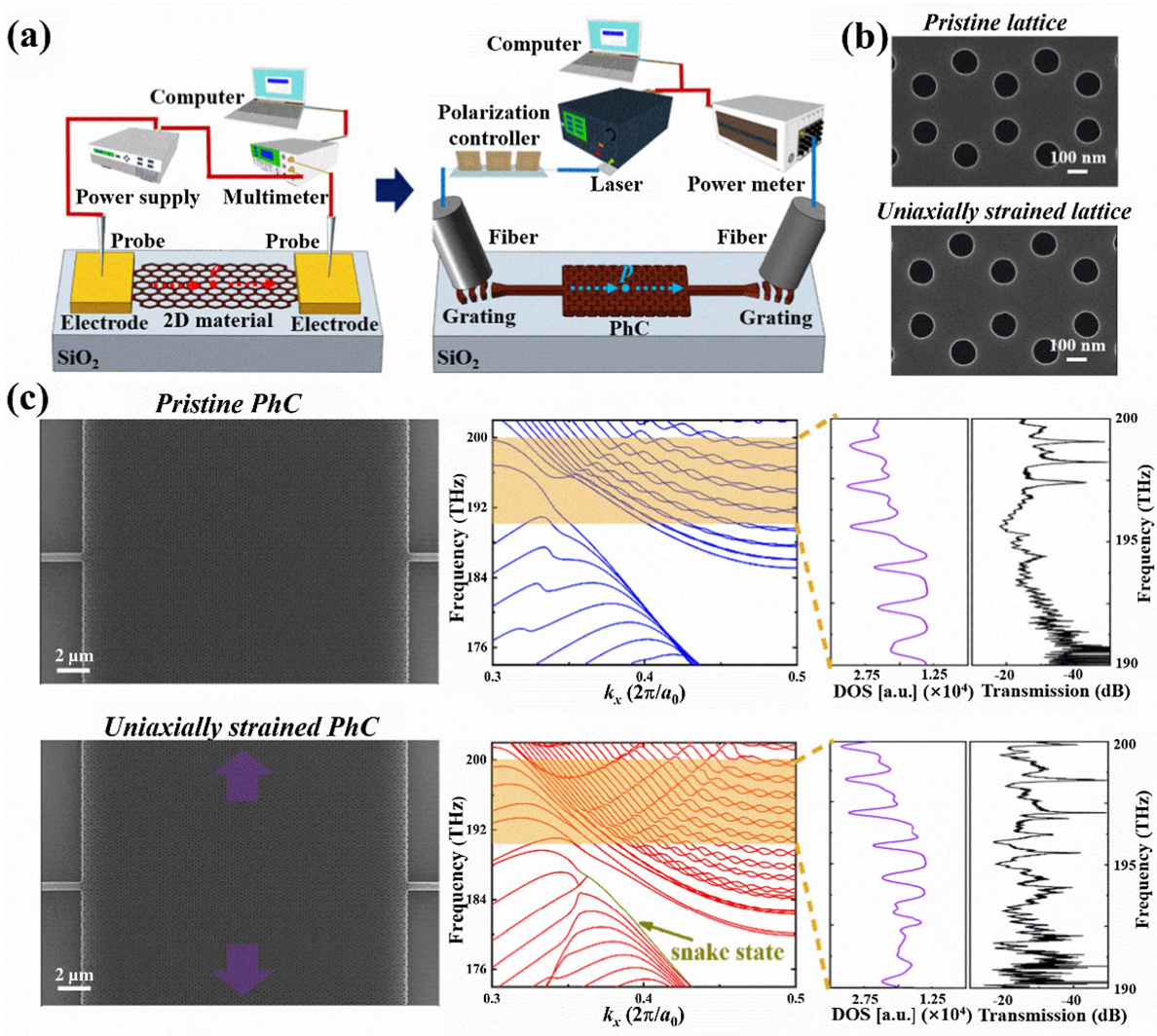

Fig. 3. Optical transports in the uniaxially strained PhC. (a) Left: Electrical measurement setup for the 2D materials. Right: Optical measurement setup for the Si-based PhC with the integration of Si waveguides and gratings. (b) SEM images of the pristine photonic lattices and the uniaxially strained photonic lattices with $u_0 = 0.04$. (c) From left to right: SEM images, simulated band diagrams, calculated photonic DOS, and measured transmission spectra for the pristine and the uniaxially strained PhCs, respectively.

snake state is protected by the winding topology of the Landau level [60,61]. Thus, such a snake optical mode could maintain cyclotron motion without significant backscattering and reflections until it reaches the right end of the PhC.

To manipulate the flow of light in the topological photonic nanostructures, adopting unidirectional coupling is one of the most common methods. It is totally accessible to achieve the high-efficiency unidirectional coupling based on the circularly polarized light sources to valley-dependent topological interfaces, enabling the generation of an optical vortex in the valley kink states [62]. Similarly, we used a microdisk with a diameter of 2 μm, as depicted in Fig. 4(c), to produce the vortex fields. This microdisk was located at the left end of the proposed PhC and on the same line as the domain wall, which could couple the TE waves from the Si waveguide into the right clockwise-polarized (RCP) or left clockwise-polarized (LCP) light. It should be emphasized that the snake state is a kind of helical edge state [63]. Because of the conserved time-reversal symmetry under $\boldsymbol{B}_s$, the snake states that correspond to different valleys could propagate in opposite directions, contributing to the helical transports. And, without the limit of valley-chirality locking [64], there is no need to break the inversion symmetry of the domain wall to inspire the snake modes. The helicity ensures the inspiration of the snake modes by using either RCP or LCP light sources. Both the simulated and the measured transmission spectra have been presented in Fig. 4(d), which shows the transmitted power goes high with the wavelength exceeding 1600 nm and demonstrates the successful inspiration of the helical snake state modes in the uniaxially strained PhC. Meanwhile, only one transmission dip can be observed in the wavelength range of 1500–1560 nm, which is induced by the optical resonance in the microdisk. Compared to direct coupling, unidirectional coupling shows a much lower efficiency in the inspiration of bulk modes due to a kinetic

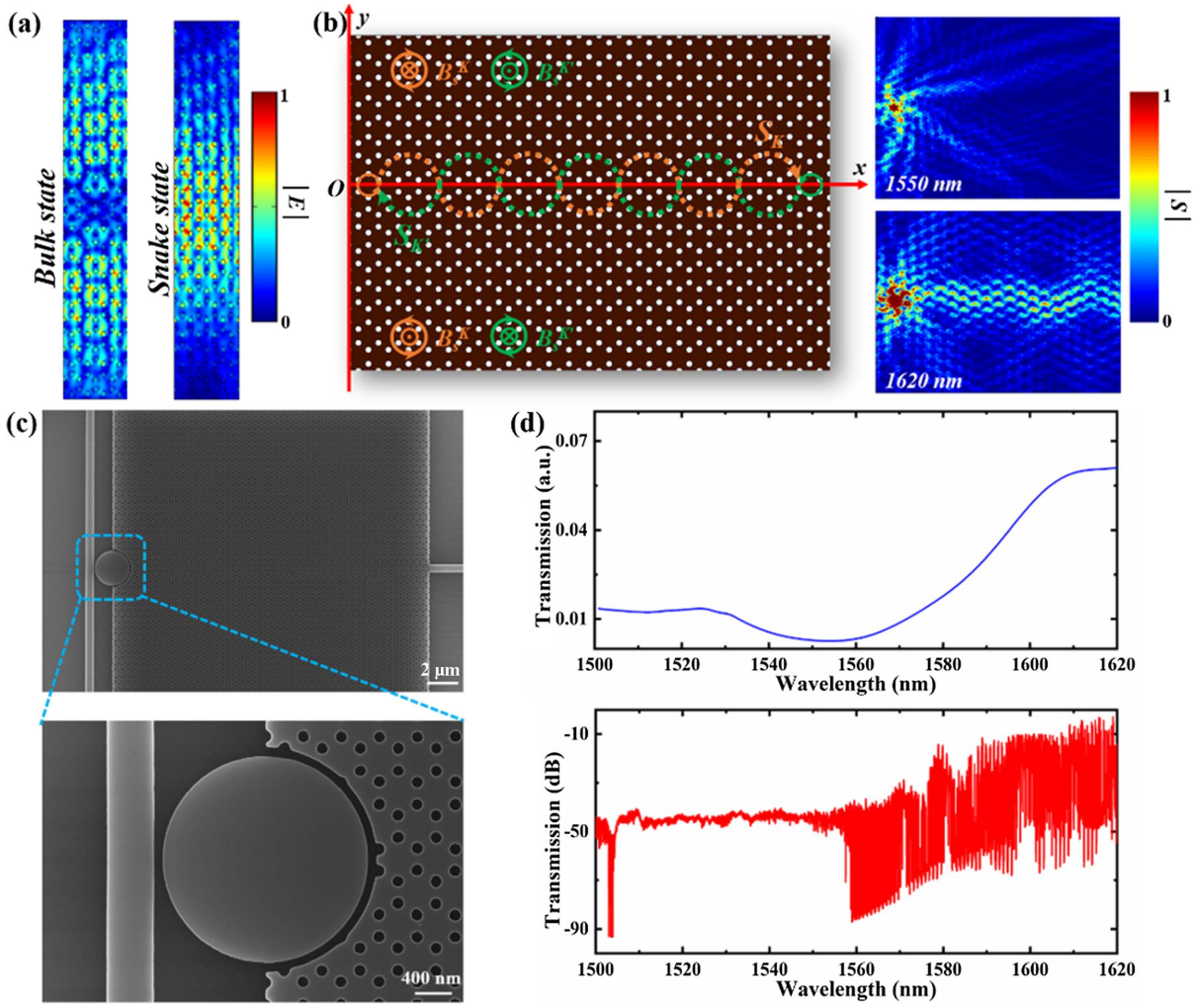

Fig. 4. Inspiration of helical snake states. (a) Electric field distributions of the bulk mode and the snake state mode in the uniaxially strained PhC. (b) Left: Illustration of the counterpropagating lightwaves (S_K and $S_{K'}$) with the snake orbits along the undeformed lattices of the uniaxially strained PhC based on the excitations of circularly polarized light sources. Right: FDTD simulations of the unidirectional coupling by introducing the LCP dipole source at $\lambda = 1550$ nm and 1620 nm, respectively. (c) SEM images of the sample coupled with a microdisk at its left end. The input Si waveguide is directionally coupled to such microdisk, and the air gap is nearly 100 nm. (d) Simulated and measured transmission spectra for the sample under the excitation of circularly polarized light.

mismatch, as shown in Fig. 4(b). In addition, the noises are greatly enhanced when the input wavelength is beyond 1570 nm since the optimal operation range of the Si grating is from 1500 to 1570 nm.

C. Electrical Manipulation of the Photonic DOS

We have also verified the electrical manipulation of the photonic DOS for the uniaxially strained PhC on the SOI platform. A 100 nm thick TiN heat electrode is deposited onto the SiO_2 upper cladding layer, which owns excellent electrical as well as thermal conductivities. The refractive index (RI) of Si is highly sensitive to the heat generated by the TiN electrode due to its large thermo-optic coefficient ($\sim 1.84 \times 10^{-4}$ K^{-1} at room temperature) [65]. Once a certain voltage is applied onto the electrodes, the RIs of Si and SiO_2 will change due to the Joule heat-induced temperature variations, influencing the band structure of the proposed PhC. This could further lead to shifts in the transmission dips because of the variations in the photonic DOS. As schematically illustrated in Fig. 5(a), we established an optoelectronic experimental setup to electrically manipulate the optical transports in the uniaxially strained PhC. A direct current (DC) power supply was used to connect the two probes that have contact with the 50 μm × 50 μm square electrode pads. Figure 5(b) shows that the heat part of the electrode is in the middle of the PhC with a size of around 45 μm × 15 μm, which is rectangular and buried into the SiO_2 upper cladding layer in case of heat dissipation and oxidation. The vertical distance between the heat electrode and the PhC (~1.8 μm) is large enough to avoid metallic absorptions for the propagating lightwaves. The resistance of the electrode is nearly 125 Ω.

The calculated photonic DOS and the experimentally measured transmission spectra with different applied DC voltages (V_{DC}) are shown in Fig. 5(c). The positions of the DOS peaks could match well with those of the transmission dips even

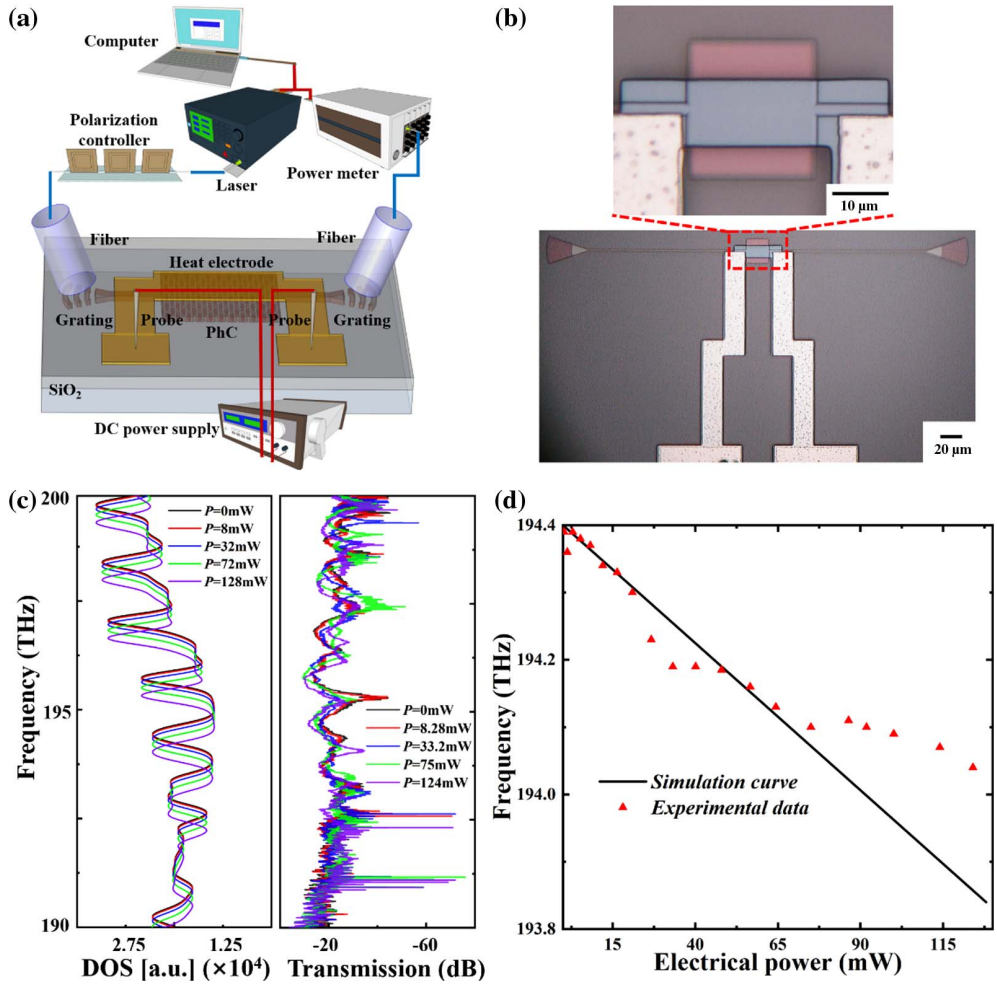

Fig. 5. Electrical manipulation of lightwaves in the uniaxially strained PhC. (a) Optoelectronic measurement setup for the sample. (b) Microscope images of the sample with the integration of heat electrodes. (c) Calculated photonic DOS and measured transmission spectra for the uniaxially strained PhC with different heating powers of 0, 8, 32, 72, and 128 mW, respectively. (d) Frequency shifts of the photonic DOS peak and the measured transmission dip at around 194.3 THz as a function of the applied electrical power.

under different V_{DC}. In addition, there is an obvious red shift in the transmission dips when the heating power (or V_{DC}) is increased from 0 to 124 mW (or 4 V), revealing the successful electrical manipulation of the photonic DOS in the uniaxially strained PhC. Our simulation results show that the temperature variation in the Si-based PhC linearly varies with a change in the heating power, which is nearly 0.5 K/mW. Thus, a small V_{DC} (<1 V) can hardly give rise to high-enough heating power (<8 mW), which could only induce a few temperature variations in the Si layer. With V_{DC} (or heating power) increasing above 2 V (or 32 mW), significant shifts in the transmission dips to the lower frequency can be observed. Meanwhile, the relationship between the frequency shift and the heating power is also linear, as indicated by the black solid line in Fig. 5(d), which is theoretically calculated to be 0.0044 THz/mW. However, the calculated value is still a bit larger than the experimentally measured one that is averaged to be 0.0028 THz/mW. This is because the actual heating efficiency is lower than the simulated one. As depicted in Fig. 5(b), the heat electrode cannot totally cover the proposed PhC, indicating that the actual heat-induced temperature variation in the configuration should be smaller than the estimated value, especially when the heating power is high. It is believed that a more effective electrical manipulation of the photonic DOS can be obtained by improving the electrode structures. Furthermore, the proposed thermo-optical control method is easy to realize, which can also be applied to the triaxially strained photonic honeycomb lattices.

3. CONCLUSIONS

In this work, we achieved $\boldsymbol{B}_s$ for the on-chip optical transports in the uniaxially strained photonic honeycomb lattices on an SOI substrate. Benefiting from the $\boldsymbol{B}_s$-induced energy states and flat plateaus for the bulk modes, the photonic DOS of the sample has been detected by measuring the transmission spectra. Through adopting the microdisk for the unidirectional coupling, the helical snake modes are inspired at the undeformed part (middle) of the uniaxially strained PhC. Such helical snake states provide a promising platform to design

Si-based topological photonic waveguides operating at telecom wavelengths without breaking the time-reversal symmetry. Significantly, we used heat electrodes to electrically manipulate the photonic DOS in the uniaxially strained PhC for what we believe is the first time, to the best of our knowledge, which revealed that $\boldsymbol{B}_s$ could be subject to electrical modulations. This paves the way for the application of on-chip $\boldsymbol{B}_s$-related functional optical devices involving switches and modulators, which can also be extended to other integrated systems based on terahertz or elastic waves. Our study not only realizes $\boldsymbol{B}_s$ by exerting a linear parabolic deformation on the honeycomb lattices but enables lightwave manipulation in the near-IR region, showing a great prospect to build lab-on-chips to investigate strongly correlated light–matter interactions and integrated photonic circuits to support chip-scale optical communications.

Funding. National Natural Science Foundation of China (62105158, 62075038, 12104233, 12004189); Natural Science Foundation of Jiangsu Province (BK20210645); Natural Science Research of Jiangsu Higher Education Institutions of China (21KJB140012); Innovation and Entrepreneurship Program of Jiangsu Province (JSSCBS20210467); Key Research and Development Program of Jiangsu Province (BE2021667).

Disclosures. The authors declare no conflicts of interests.

Data Availability. Data underlying the results presented in this paper are not publicly available at this time but may be obtained from the authors upon reasonable request.

REFERENCES

1. K. S. Novoselov, Z. Jiang, Y. Zhang, S. V. Morozov, H. L. Stormer, U. Zeitler, J. C. Maan, G. S. Boebinger, P. Kim, and A. K. Geim, "Room-temperature quantum Hall effect in graphene," Science **315**, 1379 (2007).
2. K. V. Klitzing, G. Dorda, and M. Pepper, "New method for high-accuracy determination of the fine-structure constant based on quantized Hall resistance," Phys. Rev. Lett. **45**, 494–497 (1980).
3. Y. Hatsugai, "Chern number and edge states in the integer quantum Hall effect," Phys. Rev. Lett. **71**, 3697–3700 (1993).
4. F. Guinea, M. I. Katsnelson, and A. K. Geim, "Energy gaps and a zero-field quantum Hall effect in graphene by strain engineering," Nat. Phys. **6**, 30–33 (2010).
5. M. M. Fogler, F. Guinea, and M. I. Katsnelson, "Pseudomagnetic fields and ballistic transport in a suspended graphene sheet," Phys. Rev. Lett. **101**, 226804 (2008).
6. M. Mucha-Kruczyński and V. I. Falko, "Pseudo-magnetic field distribution and pseudo-Landau levels in suspended graphene flakes," Solid State Commun. **152**, 1442–1445 (2012).
7. H. Sun, Z. Qi, Y. Kim, M. Luo, B. Yang, and D. Nam, "Frequency-tunable terahertz graphene laser enabled by pseudomagnetic fields in strain-engineered graphene," Opt. Express **29**, 1892–1902 (2021).
8. N. Levy, S. A. Burke, K. L. Meaker, M. Panlasigui, A. Zettl, F. Guinea, A. H. C. Neto, and M. F. Crommie, "Strain-induced pseudo-magnetic fields greater than 300 tesla in graphene nanobubbles," Science **329**, 544–547 (2010).
9. M. R. Masir, D. Moldovan, and F. M. Peeters, "Pseudo magnetic field in strained graphene: revisited," Solid State Commun. **175**, 76–82 (2013).
10. T. Low and F. Guinea, "Strain-induced pseudomagnetic field for novel graphene electronics," Nano Lett. **10**, 3551–3554 (2010).
11. C. Si, Z. Sun, and F. Liu, "Strain engineering of graphene: a review," Nanoscale **8**, 3207–3217 (2016).
12. F. Guinea, A. K. Geim, M. I. Katsnelson, and K. S. Novoselov, "Generating quantizing pseudomagnetic fields by bending graphene ribbons," Phys. Rev. B **81**, 035408 (2010).
13. D. B. Zhang, G. Seifert, and K. Chang, "Strain-induced pseudomagnetic fields in twisted graphene nanoribbons," Phys. Rev. Lett. **112**, 096805 (2014).
14. C. C. Hsu, M. L. Teague, J. Q. Wang, and N. C. Yeh, "Nanoscale strain engineering of giant pseudo-magnetic fields, valley polarization, and topological channels in graphene," Sci. Adv. **6**, eaat9488 (2020).
15. D. H. Kang, H. Sun, M. Luo, K. Lu, M. Chen, Y. Kim, Y. Jung, X. Gao, S. J. Parluhutan, J. Ge, S. W. Koh, D. Giovanni, T. C. Sum, Q. J. Wang, H. Li, and D. Nam, "Pseudo-magnetic field-induced slow carrier dynamics in periodically strained graphene," Nat. Commun. **12**, 5087 (2021).
16. J. Mornhinweg, M. Halbhuber, C. Ciuti, D. Bougeard, R. Huber, and C. Lange, "Tailored subcycle nonlinearities of ultrastrong light-matter coupling," Phys. Rev. Lett. **126**, 177404 (2021).
17. S. Rajabali, E. Cortese, M. Beck, S. De Liberato, J. Faist, and G. Scalari, "Polaritonic nonlocality in light–matter interaction," Nat. Photonics **15**, 690–695 (2021).
18. D. De Bernardis, Z. P. Cian, I. Carusotto, M. Hafezi, and P. Rabl, "Light–matter interactions in synthetic magnetic fields: Landau-photon polaritons," Phys. Rev. Lett. **126**, 103603 (2021).
19. E. M. Purcell, H. C. Torrey, and R. V. Pound, "Resonance absorption by nuclear magnetic moments in a solid," Phys. Rev. **69**, 37–38 (1946).
20. G. Scalari, C. Maissen, D. Turčinková, D. Hagenmüller, S. De Liberato, C. Ciuti, C. Reichl, D. Schuh, W. Wegscheider, M. Beck, and J. Faist, "Ultrastrong coupling of the cyclotron transition of a 2D electron gas to a THz metamaterial," Science **335**, 1323–1326 (2012).
21. J. Yuan, C. Xu, H. Cai, and D. W. Wang, "Gap-protected transfer of topological defect states in photonic lattices," APL Photon. **6**, 030803 (2021).
22. N. Schine, M. Chalupnik, T. Can, A. Gromov, and J. Simon, "Electromagnetic and gravitational responses of photonic Landau levels," Nature **565**, 173–179 (2019).
23. M. Hafezi, E. A. Demler, M. D. Lukin, and J. M. Taylor, "Robust optical delay lines with topological protection," Nat. Phys. **7**, 907–912 (2011).
24. F. Deng, Y. Li, Y. Sun, X. Wang, Z. Guo, Y. Shi, H. Jiang, K. Chang, and H. Chen, "Valley-dependent beams controlled by pseudomagnetic field in distorted photonic graphene," Opt. Lett. **40**, 3380–3383 (2015).
25. E. Plum, X. X. Liu, V. A. Fedotov, Y. Chen, D. P. Tsai, and N. I. Zheludev, "Metamaterials: optical activity without chirality," Phys. Rev. Lett. **102**, 113902 (2009).
26. Y. Ming and C. W. Qiu, "Zero chiral bulk modes in 3D Weyl metamaterials," Sci. Bull. **64**, 799–801 (2019).
27. H. Jia, R. Zhang, W. Gao, Q. Guo, B. Yang, J. Hu, Y. Bi, Y. Xiang, C. Liu, and S. Zhang, "Observation of chiral zero mode in inhomogeneous three-dimensional Weyl metamaterials," Science **363**, 148–151 (2019).
28. M. Hafezi, S. Mittal, J. Fan, A. Migdall, and J. M. Taylor, "Imaging topological edge states in silicon photonics," Nat. Photonics **7**, 1001–1005 (2013).
29. N. Schine, A. Ryou, A. Gromov, A. Sommer, and J. Simon, "Synthetic Landau levels for photons," Nature **534**, 671–675 (2016).
30. H. Schomerus and N. Y. Halpern, "Parity anomaly and Landau-level lasing in strained photonic honeycomb lattices," Phys. Rev. Lett. **110**, 013903 (2013).
31. J. Guglielmon, M. C. Rechtsman, and M. I. Weinstein, "Landau levels in strained two-dimensional photonic crystals," Phys. Rev. A **103**, 013505 (2021).
32. M. C. Rechtsman, J. M. Zeuner, A. Tünnermann, S. Nolte, M. Segev, and A. Szameit, "Strain-induced pseudomagnetic field and photonic Landau levels in dielectric structures," Nat. Photonics **7**, 153–158 (2013).
33. Z. Yang, F. Gao, Y. Yang, and B. Zhang, "Strain-induced gauge field and Landau levels in acoustic structures," Phys. Rev. Lett. **118**, 194301 (2017).

34. O. Jamadi, E. Rozas, G. Salerno, M. Milićević, T. Ozawa, I. Sagnes, A. Lemaître, L. Le Gratiet, A. Harouri, I. Carusotto, J. Bloch, and A. Amo, "Direct observation of photonic Landau levels and helical edge states in strained honeycomb lattices," Light Sci. Appl. **9**, 144 (2020).
35. G. J. Verbiest, S. Brinker, and C. Stampfer, "Uniformity of the pseudomagnetic field in strained graphene," Phys. Rev. B **92**, 075417 (2015).
36. D. N. Le, V. H. Le, and P. Roy, "Graphene under uniaxial inhomogeneous strain and an external electric field: Landau levels, electronic, magnetic and optical properties," Eur. Phys. J. B **93**, 38–40 (2020).
37. S. Zhu, J. A. Stroscio, and T. Li, "Programmable extreme pseudomagnetic fields in graphene by a uniaxial stretch," Phys. Rev. Lett. **115**, 245501 (2015).
38. M. Yan, W. Deng, X. Huang, Y. Wu, Y. Yang, J. Lu, F. Li, and Z. Liu, "Pseudomagnetic fields enabled manipulation of on-chip elastic waves," Phys. Rev. Lett. **127**, 136401 (2021).
39. M. Teng, S. Fathpour, R. Safian, L. Zhuang, A. Honardoost, Y. Alahmadi, S. S. Polkoo, K. Kojima, H. Wen, C. K. Renshaw, P. Likamwa, and G. Li, "Miniaturized silicon photonics devices for integrated optical signal processors," J. Lightwave Technol. **38**, 6–17 (2020).
40. J. Qin, S. Jiang, Z. Wang, X. Cheng, B. Li, Y. Shi, D. P. Tsai, A. Q. Liu, W. Huang, and W. Zhu, "Metasurface micro/nano-optical sensors: principles and applications," ACS Nano **16**, 11598–11618 (2022).
41. T. Nagatsuma, G. Ducournau, and C. C. Renaud, "Advances in terahertz communications accelerated by photonics," Nat. Photonics **10**, 371–379 (2016).
42. Y. A. Vlasov, M. O'Boyle, H. F. Hamann, and S. J. McNab, "Active control of slow light on a chip with photonic crystal waveguides," Nature **438**, 65–69 (2005).
43. S. Noda, K. Kitamura, T. Okino, D. Yasuda, and Y. Tanaka, "Photonic-crystal surface-emitting lasers: review and introduction of modulated-photonic crystals," IEEE J. Sel. Top. Quantum Electron. **23**, 4900107 (2017).
44. G. Shambat, B. Ellis, A. Majumdar, J. Petykiewicz, M. A. Mayer, T. Sarmiento, J. Harris, E. E. Haller, and J. Vučković, "Ultrafast direct modulation of a single-mode photonic crystal nanocavity light-emitting diode," Nat. Commun. **2**, 539 (2011).
45. Z. Qi, G. Hu, C. Deng, H. Sun, Y. Sun, Y. Li, B. Liu, Y. Bai, S. Chen, and Y. Cui, "Electrical tunable topological valley photonic crystals for on-chip optical communications in the telecom band," Nanophotonics **11**, 4273–4285 (2022).
46. S. H. Lee, M. Choi, T. T. Kim, S. Lee, M. Liu, X. Yin, H. K. Choi, S. S. Lee, C. G. Choi, S. Y. Choi, X. Zhang, and B. Min, "Switching terahertz waves with gate-controlled active graphene metamaterials," Nat. Mater. **11**, 936–941 (2012).
47. C. Wang, W. Liu, Z. Li, H. Cheng, Z. Li, S. Chen, and J. Tian, "Dynamically tunable deep subwavelength high-order anomalous reflection using graphene metasurfaces," Adv. Opt. Mater. **6**, 1701047 (2018).
48. Q. Li, X. Cai, T. Liu, M. Jia, Q. Wu, H. Zhou, H. Liu, Q. Wang, X. Ling, C. Chen, F. Ding, Q. He, Y. Zhang, S. Xiao, and L. Zhou, "Gate-tuned graphene meta-devices for dynamically controlling terahertz wavefronts," Nanophotonics **11**, 2085–2096 (2022).
49. J.-M. Lourtioz, H. Benisty, V. Berger, J.-M. Gerard, D. Maystre, and A. Tchelnokov, *Photonic Crystals: Towards Nanoscale Photonic Devices* (Springer, 2005).
50. G. Montambaux, F. Piéchon, J. N. Fuchs, and M. O. Goerbig, "Merging of Dirac points in a two-dimensional crystal," Phys. Rev. B **80**, 153412 (2009).
51. V. M. Pereira, A. H. Castro Neto, and N. M. R. Peres, "Tight-binding approach to uniaxial strain in graphene," Phys. Rev. B **80**, 045401 (2009).
52. P. Ruffieux, S. Wang, B. Yang, C. Sanchez-Sanchez, J. Liu, T. Dienel, L. Talirz, P. Shinde, C. A. Pignedoli, D. Passerone, T. Dumslaff, X. Feng, K. Müllen, and R. Fasel, "On-surface synthesis of graphene nanoribbons with zigzag edge topology," Nature **531**, 489–492 (2016).
53. A. Chaves, L. Covaci, K. Y. Rakhimov, G. A. Farias, and F. M. Peeters, "Wave-packet dynamics and valley filter in strained graphene," Phys. Rev. B **82**, 205430 (2010).
54. M. Jamotte, N. Goldman, and M. Di Liberto, "Strain and pseudomagnetic fields in optical lattices from density-assisted tunneling," Commun. Phys. **5**, 30 (2022).
55. H. T. Yang, "Strain induced shift of Dirac points and the pseudomagnetic field in graphene," J. Phys. Condens. Matter **23**, 505502 (2011).
56. M. Luo, H. Sun, Z. Qi, K. Lu, M. Chen, D. Kang, Y. Kim, D. Burt, X. Yu, C. Wang, Y. D. Kim, H. Wang, Q. J. Wang, and D. Nam, "Triaxially strained suspended graphene for large-area pseudo-magnetic fields," Opt. Lett. **47**, 2174–2177 (2022).
57. K. Ohtaka, "Density of states of slab photonic crystals and the laser oscillation in photonic crystals," J. Lightwave Technol. **17**, 2161–2169 (1999).
58. J. W. Dong, X. D. Chen, H. Zhu, Y. Wang, and X. Zhang, "Valley photonic crystals for control of spin and topology," Nat. Mater. **16**, 298–302 (2017).
59. J. Lu, C. Qiu, L. Ye, X. Fan, M. Ke, F. Zhang, and Z. Liu, "Observation of topological valley transport of sound in sonic crystals," Nat. Phys. **13**, 369–374 (2017).
60. E. Tang and L. Fu, "Strain-induced partially flat band, helical snake states and interface superconductivity in topological crystalline insulators," Nat. Phys. **10**, 964–969 (2014).
61. Y. Liu, R. P. Tiwari, M. Brada, C. Bruder, F. V. Kusmartsev, and E. J. Mele, "Snake states and their symmetries in graphene," Phys. Rev. B **92**, 235438 (2015).
62. X. T. He, E. T. Liang, J. J. Yuan, H. Y. Qiu, X. D. Chen, F. L. Zhao, and J. W. Dong, "A silicon-on-insulator slab for topological valley transport," Nat. Commun. **10**, 872 (2019).
63. G. Salerno, T. Ozawa, H. M. Price, and I. Carusotto, "Propagating edge states in strained honeycomb lattices," Phys. Rev. B **95**, 245418 (2017).
64. J. Lu, C. Qiu, M. Ke, and Z. Liu, "Valley vortex states in sonic crystals," Phys. Rev. Lett. **116**, 093901 (2016).
65. J. Komma, C. Schwarz, G. Hofmann, D. Heinert, and R. Nawrodt, "Thermo-optic coefficient of silicon at 1550 nm and cryogenic temperatures," Appl. Phys. Lett. **101**, 041905 (2012).